6 Effect of Charge Self-Consistency in Calculations for Transition-Metal Oxides

Claude Ederer
Materials Theory
ETH Zürich

Contents

E. Pavarini, E. Koch, A. Lichtenstein, and D. Vollhardt (eds.)
Understanding Correlated Materials with DMFT
Modeling and Simulation Vol. 15
Forschungszentrum Jülich, 2025, ISBN 978-3-95806-813-1
http://www.cond-mat.de/events/correl25

1 Introduction

Soon after the emergence of dynamical mean-field theory (DMFT) as a powerful approach to address models of interacting fermions on a lattice, the idea emerged to combine DMFT also with realistic electronic structure calculations using density functional theory (DFT) in the local density approximation (LDA) [1, 2]. Thereby, the auxiliary independent-particle Kohn-Sham (KS) band-structure obtained within LDA is taken as a "zeroth order" approximation to the interacting problem [1]. After constructing a minimal tight-binding (TB) representation of the most relevant bands, a local electron-electron interaction is added to the corresponding Hamiltonian, resulting in a realistic materials-specific multi-orbital Hubbard model. For the case of transition metal (TM) oxides or related materials, these "most relevant bands" generally consist of partially filled bands around the Fermi level with dominant TM d orbital character, and sometimes also of bands with strong O p orbital character. Thus, a TB representation of these bands is typically based on localized d-like orbitals centered on the TM sites, and potentially also p-like orbitals on the O atoms or other anionic ligands.

The basic idea is similar in spirit to the DFT+U method [3,4], where the underlying energy functional and the KS potential are supplemented by terms explicitly describing the local electron-electron interaction within a subset of electrons, typically corresponding to localized d or f states. However, while the local interaction within DFT+U is treated on the level of a *static* mean-field approximation, within the DFT+DMFT approach the resulting multi-band Hubbard model is treated by considering a *dynamical* mean-field.[1] Thereby, each interacting site on the lattice is viewed as an individual atom that is embedded in an effective bath. Thus, the bath in principle consists of all other atoms in the system. Electrons can dynamically fluctuate between the selected atom and the bath. Electrons on the atom interact with each other via the local electron-electron interaction, while electrons in the bath are considered as non-interacting. Thus, the original lattice problem is mapped to an Anderson-type impurity problem. However, since the bath of this effective impurity problem indeed consists of all other sites, which are either equivalent to the selected site or connected to it via their respective effective baths, the bath itself is related to the solution of the impurity problem via a self-consistency condition.

The fact that this approach has evolved into a powerful method that is nowadays also applied to the treatment of rather complex materials systems involving, e.g., heterostructures, surfaces, or point defects (see, e.g., [5–7]), is closely tied to the availability of efficient and accurate computational methods to solve the corresponding Anderson impurity problem(s). Various examples of such *impurity solvers* have been discussed in other lecture notes within this series and therefore will not be discussed here. We just note that the effect of the bath, the hybridization between the bath and the impurity site, and the non-interacting part of the local Hamiltonian, are encoded in the form of a non-interacting local Green function, the so-called *Weiss field*, $\mathcal{G}_0$, usually expressed in a basis of suitable localized orbitals. The impurity solver then takes $\mathcal{G}_0$ as

[1] In these lecture notes, we use the term "DFT+DMFT" instead of the more traditional "LDA+DMFT", acknowledging the fact that many calculations are nowadays using DFT functionals based on the generalized gradient approximation or other semi-local exchange correlation (xc) functionals. Thus, "DFT" in "DFT+DMFT" should be read as "DFT using some approximate semi-local xc functional".

input, together with the specific form of the local interaction Hamiltonian, $\hat{H}_{\text{int}}$, and computes the full one-particle Green function of the impurity, G^{imp} as well as the local impurity self energy, Σ^{imp}, which are related via the Dyson equation $(G^{\text{imp}})^{-1} = \mathcal{G}_0^{-1} - \Sigma^{\text{imp}}$. The impurity self energy is then used as purely local approximation to the self energy of the original lattice problem, and a new estimate of the Weiss field can be obtained from the local component of the lattice Green function. This procedure, described in more detail in Sec. 2, is then repeated until a self-consistent solution is obtained, such that the local part of the lattice Green function becomes identical to the impurity Green function.

In most realistic cases, the DMFT treatment of the local interaction results in a redistribution of electrons compared to the underlying initial DFT calculation. For example, in systems where a local crystal field splitting lifts the degeneracy between partially filled d levels, electrons can be redistributed between the different non-degenerate orbitals, and in complex crystal structures, where several inequivalent atomic sites are mapped on different effective impurity problems, electrons can be redistributed between different sites. This redistribution of electrons corresponds to a change in the electronic charge density of the system, which consequently also changes the KS potential that was used in the initial DFT calculation, and thus also the corresponding band structure changes compared to the initial bandstructure that was used to construct the multi-orbital Hubbard model for the DMFT treatment. Therefore, in order to arrive at a truly realistic and potentially also quantitative and predictive method for the treatment of complex correlated materials, an additional self-consistency over the charge density is required. Furthermore, if quantities related to total energy differences are of interest, then the condition for stationarity of the underlying energy functional also demands *charge self-consistency*.

However, charge self-consistency increases the required computational effort and simultaneously also increases the complexity of the computational scheme, since DFT calculations have to be performed for which the KS potential is calculated from an externally modified charge density, and the information about this modified charge density has to be transferred from the DMFT part of the calculation to the DFT code that is used. Therefore, in practice, charge self-consistency is often neglected in favor of so-called "one-shot" calculations, where the DMFT calculation is essentially a "post-processing" of the DFT results, and the DFT calculation is merely providing a fixed input to the DMFT part. It is therefore essential to be aware of the potential limitations of such one-shot calculations, and to recognize cases that require the full charge self-consistent treatment.

In these lecture notes, we present several case studies of DFT+DMFT calculations for specific materials where charge self-consistency is important and leads to noticeable differences from the one-shot results. However, before discussing the various examples in Sec. 4, we start with a detailed description of the charge self-consistent DFT+DMFT approach, which is presented in Sec. 2. Thereby, we emphasize a clear and transparent definition of what represents "the most relevant bands", and show how all relevant quantities can be transformed back and forth between the KS Bloch basis and the localized orbitals centered on the relevant sites, which is required for a fully charge self-consistent treatment. We also briefly discuss how the DFT+DMFT approach can be derived from a specific approximation to the Gibbs free energy functional, providing

a solid theoretical foundation of the method. Then, before discussing the several examples demonstrating the effect of charge self-consistency, a brief summary of the most relevant aspects of TM oxides is provided in Sec. 3, which is intended to help to better understand the different materials aspects in the various case studies.

2 Charge self-consistent DFT+DMFT

2.1 Definition of the correlated subspace and Wannier functions

The main conceptual idea behind DFT+DMFT as a "first principles"-based method for quantitative materials-specific electronic structure calculations, is based on a separation of the electronic degrees of freedom into a strongly interacting and a weakly interacting part. The basic assumption is, that the weakly interacting subspace, which makes up the largest part of the electronic Hilbert space, is well described by DFT using standard local or semi-local exchange-correlation functionals, and that only a small subset of electronic degrees of freedom, the *correlated subspace*, $\mathcal{C}$, requires a more sophisticated treatment of the local electron-electron interaction. The correlated subspace typically involves partially filled bands around the Fermi level corresponding to relatively localized orbital degrees of freedom. The assumption that a more sophisticated treatment is only necessary for a small subset of electrons, is of course to some extent also a matter of necessity, since a full treatment of all electronic degrees of freedom within DMFT (or another more advanced computational many-body approach) is not realistically feasible.

In the case of transition metal oxides, the correlated subspace typically consists of the "d electrons" corresponding to the transition metal ions with partially filled d shell, or of a subset thereof, such as, e.g., either the e_g or t_{2g} subshells in systems with a pronounced octahedral crystal field splitting. However, it should be noted that, as discussed also in some detail in Sec. 3, there is some ambiguity what is meant by the "d electrons" in a specific material, reflecting the fact that local angular momentum is not a good quantum number in a periodic solid. The choice of the correlated subspace for a specific material is therefore always to some degree based on physical and chemical intuition, or other specific insights on what are the most important degrees of freedom that require a treatment beyond conventional DFT. The obtained results will generally depend on this choice. Nevertheless, in many cases it has been found that even somewhat different but reasonable choices can lead to consistent results.

The correlated subspace is typically defined in terms of a set of orthogonal spatially localized orbitals, $|\phi_{m\mathbf{T}}\rangle$, centered on specific sites within each crystallographic unit cell, in the following called the "correlated sites". $\mathbf{T}$ is a vector of the underlying Bravais lattice and indicates the crystallographic unit cell where the corresponding orbital is located, while m represents the orbital character including spin. In cases with more than one correlated site per unit cell, m indicates both the specific site within the unit cell as well as the corresponding orbital character. For transition metal oxides, the correlated sites typically coincide with the positions of the transition metal cations.

It is convenient to work with Bloch sums, i.e., Fourier transforms, of the local orbitals, defined

as follows

$$|\phi_{m\mathbf{k}}\rangle = \sum_{\mathbf{T}} e^{i\mathbf{k}\cdot\mathbf{T}}|\phi_{m\mathbf{T}}\rangle \quad \leftrightarrow \quad |\phi_{m\mathbf{T}}\rangle = \frac{V}{(2\pi)^3}\int_{\mathrm{BZ}} d\mathbf{k}\, e^{-i\mathbf{k}\cdot\mathbf{T}}|\phi_{m\mathbf{k}}\rangle, \tag{1}$$

where the integral over $\mathbf{k}$ is taken over the Brillouin zone (BZ) of the crystal and V is the unit cell volume. Since in practice one always works with a finite set of KS Bloch states, $|\psi_{\nu\mathbf{k}}\rangle$, corresponding to a finite number of bands (indexed by ν), an arbitrary orbital generally cannot be exactly represented in this Bloch basis. Consequently, the projections of a set of given *trial orbitals* into this restricted Bloch space $\mathcal{R}$:

$$|\phi^{(\mathcal{R})}_{m\mathbf{k}}\rangle = \sum_{\nu\in\mathcal{R}} |\psi_{\nu\mathbf{k}}\rangle\langle\psi_{\nu\mathbf{k}}|\phi_{m\mathbf{k}}\rangle, \tag{2}$$

are not necessarily orthogonal to each other, even if the original trial orbitals were. However the set of $|\phi^{(\mathcal{R})}_{m\mathbf{k}}\rangle$ can always be subsequently orthogonalized, using, e.g., Löwdin orthonormalization (see, e.g., [8]). Furthermore, only the projection of $|\phi_{m\mathbf{k}}\rangle$ into $\mathcal{R}$ is relevant for the DFT+DMFT treatment. Therefore, in the following we always use the orthonormalized projections, $|\phi^{(\mathcal{R})}_{m\mathbf{k}}\rangle$, of the original trial orbitals as our local orbital basis, and we drop the superscript $\mathcal{R}$ again for ease of notation. Thus, from now on we can assume that the $|\phi_{m\mathbf{k}}\rangle$ form an orthonormal basis and are completely representable in $\mathcal{R}$.

A set of localized orbitals that exhibits this property automatically by construction are *Wannier functions* [8], defined as

$$|w_{m\mathbf{T}}\rangle = \frac{V}{(2\pi)^3}\int_{\mathrm{BZ}} d\mathbf{k}\, e^{-i\mathbf{k}\cdot\mathbf{T}} \sum_{\nu} U^{(\mathbf{k})}_{\nu m}|\psi_{\nu\mathbf{k}}\rangle = \frac{V}{(2\pi)^3}\int_{\mathrm{BZ}} d\mathbf{k}\, e^{-i\mathbf{k}\cdot\mathbf{T}}|w_{m\mathbf{k}}\rangle. \tag{3}$$

The functions $|w_{m\mathbf{k}}\rangle = \sum_\nu U^{(\mathbf{k})}_{\nu m}|\psi_{\nu\mathbf{k}}\rangle$ are equivalent to the Bloch sums $|\phi_{m\mathbf{k}}\rangle$ defined from the local orbitals $|\phi_{m\mathbf{T}}\rangle$ and are sometimes called "$\mathbf{k}$-space Wannier functions" or "remixed Bloch states", since they are defined as a linear combination of the Kohn-Sham eigenfunctions corresponding to a set of bands at the same $\mathbf{k}$-point. Specific Wannier functions are defined by a specific choice of the matrices $U^{(\mathbf{k})}_{\nu m}$. In fact, the procedure described above, i.e., projecting some localized trial orbitals on the Bloch space with subsequent Löwdin orthonormalization, is one widely-used approach to obtain Wannier functions, which then typically closely resemble the orbital character of the initial trial orbitals. Such Wannier functions have been termed "Wannier functions via projection" or "projected Wannier functions" [8]. Another wide-spread possibility is to minimize the total quadratic spatial spread of the Wannier functions, leading to so-called *maximally localized Wannier functions* (MLWFs) [8]. In this case, Wannier functions defined via projections are often used as starting point for the spread minimization and thus the resulting MLWFs typically also closely resemble the orbital character of the initial trial orbitals.

The summation over the band index ν in Eq. (3) is often further restricted to only a specific group of bands, which can either be completely isolated from other bands at lower and higher energies, or is defined within a certain energy window around the Fermi level. The resulting subspace is called the *Wannier space*, $\mathcal{W}$, and is a subset of $\mathcal{R}$. If the number of Bloch states

in the sum in Eq. (3) matches the number of Wannier functions, i.e., if the dimension of the correlated subspace $\mathcal{C}$ is identical to that of the Wannier space $\mathcal{W}$, then the matrices $U^{(\mathbf{k})}_{\nu m}$ are square unitary matrices for each $\mathbf{k}$, and the two subspaces are in fact identical. If the number of Bloch functions in the sum is larger than the number of Wannier functions (which is generally the case for bands that are "entangled" with other bands at lower and/or higher energies), then $\mathcal{C}$ is a subspace of $\mathcal{W}$. In this case, $\left(U^{(\mathbf{k})\dagger}\,U^{(\mathbf{k})}\right)_{mm'}=\delta_{mm'}$ still holds, while $\left(U^{(\mathbf{k})}U^{(\mathbf{k})\dagger}\right)_{\nu\nu'}\neq\delta_{\nu\nu'}$, reflecting the fact that the transformation from the Bloch to the Wannier states is well-defined, whereas the inverse transformation is not.
The relation between the localized orbitals and the Kohn-Sham Bloch states can also be encoded via so-called *projector functions*

$$P_{m\nu}(\mathbf{k}) = \left\langle \phi_{m,\mathbf{T}=0} \middle| \psi_{\nu\mathbf{k}} \right\rangle. \tag{4}$$

These projector functions are equivalent to the matrices $U^{(\mathbf{k})}_{\nu m}$ in Eq. (3), with $P_{m\nu}(\mathbf{k}) = (U^{(\mathbf{k})}_{\nu m})^*$. To be consistent with a large part of the DFT+DMFT literature, from now on we use the projector functions $P_{m\nu}(\mathbf{k})$ to define the transformation between the set of local orbitals $|\phi_{m\mathbf{k}}\rangle$ and the Kohn-Sham Bloch functions $|\psi_{\nu\mathbf{k}}\rangle$. However, we note that these local orbitals, under the condition that they are orthogonal and fully represented within $\mathcal{W}$, are nothing but Wannier functions, and can also be expressed according to Eq. (3). Analogous to what is discussed above, the projector functions are square unitary matrices if $\mathcal{C} = \mathcal{W}$, i.e. $P(\mathbf{k})\cdot P^\dagger(\mathbf{k}) = P^\dagger(\mathbf{k})\cdot P(\mathbf{k}) = \mathbb{1}$. Otherwise, $\left(P(\mathbf{k})\cdot P^\dagger(\mathbf{k})\right)_{mm'} = \delta_{mm'}$ still holds, but $\left(P^\dagger(\mathbf{k})\cdot P(\mathbf{k})\right)_{\nu\nu'} \neq \delta_{\nu\nu'}$.
Finally, we summarize the different Hilbert spaces that we have defined: i) the restricted Bloch space, $\mathcal{R}$, which contains all the Kohn-Sham states obtained in the DFT calculation. This generally comprises all occupied and a certain number of unoccupied bands. ii) the Wannier space, $\mathcal{W}$, which contains only the Kohn-Sham states that enter the definition of the local orbitals, and iii) the correlated subspace, $\mathcal{C}$, which is spanned by the local orbitals centered on the correlated sites, and in which the effective DMFT local impurity problem is formulated. Thereby, $\mathcal{C}$ is a subspace of $\mathcal{W}$, which is a subspace of $\mathcal{R}$, i.e., $\mathcal{C} \subseteq \mathcal{W} \subseteq \mathcal{R}$. In the following, mostly $\mathcal{C}$ and $\mathcal{W}$ are relevant for the DFT+DMFT treatment, whereas the part of $\mathcal{R}$ that is not contained in $\mathcal{W}$ is only indirectly affected through the change of the KS potential in the case of a charge self-consistent calculation.

2.2 The DFT+DMFT self-consistency cycle

The central quantity that is evaluated within the DFT+DMFT approach is the one-particle lattice Green function, which, expressed in the KS Bloch basis, can be written as

$$\left[G^{-1}(\mathbf{k}, i\omega_n)\right]_{\nu\nu'} = (i\omega_n + \mu - \epsilon_{\nu\mathbf{k}})\,\delta_{\nu\nu'} - \Delta\Sigma_{\nu\nu'}(\mathbf{k}, i\omega_n). \tag{5}$$

Here, ω_n is the n-th Matsubara frequency, $\omega_n = (2n+1)\pi/\beta$, with the inverse temperature $\beta = 1/T$, μ is the chemical potential, $\epsilon_{\nu\mathbf{k}}$ is the Kohn-Sham eigenvalue corresponding to $|\psi_{\nu\mathbf{k}}\rangle$, and $\Delta\Sigma_{\nu\nu'}(\mathbf{k}, i\omega_n)$ is the DMFT self-energy correction expressed in the KS basis.

The self energy correction is obtained by solving the effective impurity problems on the symmetry-inequivalent correlated sites, which are formulated in terms of the local orbital basis. The resulting impurity self energies, $\Sigma^{\text{imp}}_{mm'}(i\omega_n)$, are then *upfolded* into the Bloch basis using the projector functions $P_{m\nu}(\mathbf{k})$

$$\Delta\Sigma_{\nu\nu'}(\mathbf{k}, i\omega_n) = \sum_{mm'} [P^\dagger(\mathbf{k})]_{\nu m}\, \Delta\Sigma_{mm'}(i\omega_n)\, P_{m'\nu'}(\mathbf{k}). \tag{6}$$

Note that here a potential non-unitarity of the transformation from $\mathcal{C}$ to $\mathcal{W}$ is not a problem, since $\Delta\Sigma$ is zero by definition outside of $\mathcal{C}$. Before upfolding, one usually subtracts a double counting (DC) correction from the impurity self-energy, which is meant to contain all contributions of the local interaction within the correlated subspace that are already included in the KS potential, i.e. $\Delta\Sigma_{mm'}(i\omega_n) = \Sigma^{\text{imp}}_{mm'}(i\omega_n) - \Sigma^{\text{DC}}_{mm'}$. Typically, the DC correction is just taken to be a rigid shift of the local potential that depends on the total occupation of the local orbitals on that site, i.e., $\Sigma^{\text{DC}}_{mm'}$ is diagonal in m and depends only on the specific site related to m but not on its actual orbital character (remember that we defined m to denote both orbital character and correlated site). A specific expression for $\Sigma^{\text{DC}}_{mm'}$ is given in Sec. 2.3. Note also that the self energy in the local orbital basis is $\mathbf{k}$-independent, due to the purely local character of the effective impurity problem, whereas it gains some $\mathbf{k}$-dependence in the upfolded Bloch basis.

After performing the matrix inversion of Eq. (5) to obtain $G_{\nu\nu'}(\mathbf{k}, i\omega_n)$, the local Green function corresponding to the correlated sites is obtained by *downfolding* again back to the local orbital basis

$$G^{\text{loc}}_{mm'}(i\omega_n) = \frac{V}{(2\pi)^3} \sum_{\nu\nu'} \int d\mathbf{k}\, P_{m\nu}(\mathbf{k}) G_{\nu\nu'}(\mathbf{k}, i\omega_n) [P^\dagger(\mathbf{k})]_{\nu' m'}\,. \tag{7}$$

Here, the summation over ν and ν' can in principle be restricted over $\mathcal{W}$, since outside of $\mathcal{W}$ the projector functions are zero by definition.

The local Weiss field defining the effective local impurity problem(s) is then obtained through the Dyson equation $\mathcal{G}_0^{-1} = (G^{\text{loc}})^{-1} + \Sigma^{\text{imp}}$ (with all quantities defined as local matrices in $\mathcal{C}$, i.e., m and m' always correspond to the same correlated site). Since Σ^{imp} is in turn obtained by solving the corresponding quantum impurity problem, this defines a closed set of equations, and a self-consistent solution of this set of equations is found iteratively, as schematically depicted by the "inner" cycle in Fig. 1. If self-consistency is achieved in this inner loop, then the impurity self-energy Σ^{imp} that is obtained by solving the impurity model(s) is identical to the one from the previous iteration step that was used obtain the corresponding Weiss field(s), $\mathcal{G}_0$, and each impurity Green function is identical to the corresponding local component of the downfolded lattice Green function.

The procedure described so far corresponds to the usual DMFT self-consistency cycle for a fixed single particle Hamiltonian defined by the KS band energies $\epsilon_{\nu\mathbf{k}}$. However, since these band energies are calculated for the KS potential, and since the KS potential depends on the underlying charge density, an additional self-consistency with respect to this charge density is required.

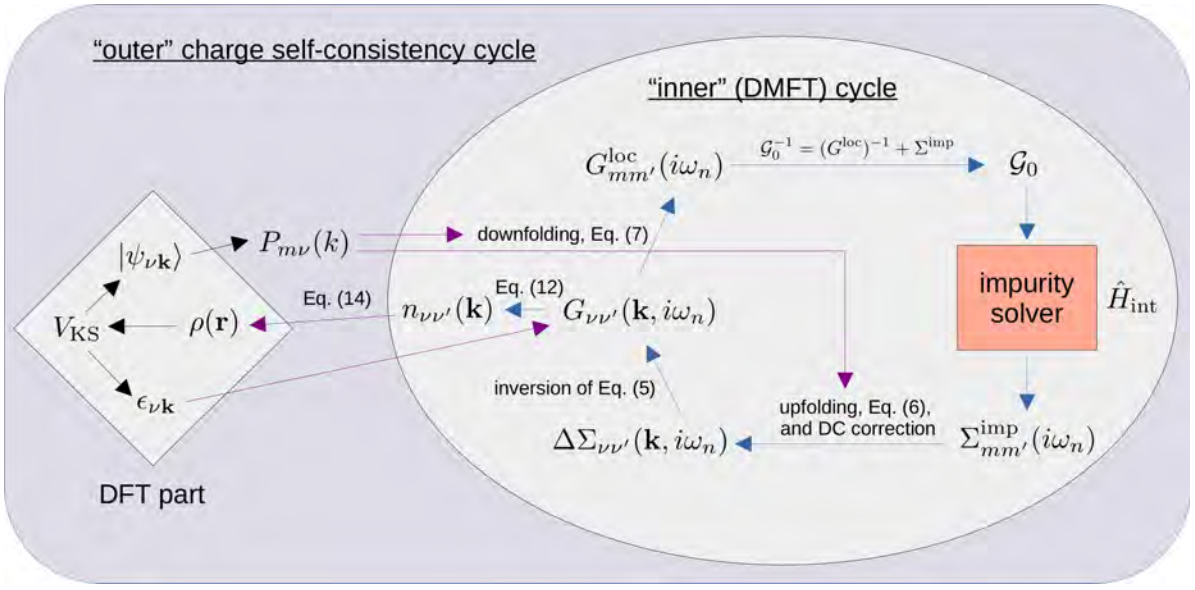

Fig. 1: *Schematic depiction of the full DFT+DMFT self-consistency cycle. The "inner loop" ensures self-consistency between the effective impurity Green function(s) and the local component(s) of the lattice Green function, while the "outer loop"ensures charge self-consistency. From the DFT perspective, the inner loop can also be viewed as a more elaborate way to obtain the occupations $n_{\nu\nu'}(\mathbf{k})$ from the solution of the KS equations.*

The charge density[2] can be obtained from the Green function in its real-space representation by summing over all Matsubara frequencies

$$\rho(\mathbf{r}) = \frac{1}{\beta} \sum_n G(\mathbf{r}, \mathbf{r}, i\omega_m). \tag{8}$$

This can easily be seen from the fundamental definition of the imaginary-time Green function in terms of field operators $\hat{\psi}(\mathbf{r}, \tau)$

$$G(\mathbf{r}, \mathbf{r}'; \tau) = -\Big\langle \hat{T}_\tau \big(\hat{\psi}(\mathbf{r}, 0) \hat{\psi}^\dagger(\mathbf{r}', \tau) \big) \Big\rangle, \tag{9}$$

where τ is imaginary time and $\hat{T}_\tau$ is the corresponding time-ordering operator. Thus, $\rho(\mathbf{r}) = G(\mathbf{r}, \mathbf{r}'; \tau{=}0^+)$, which, after Fourier transforming to Matsubara frequencies, leads to Eq. (8). Within the basis of KS Bloch states, Eq. (8) can be written as

$$\rho(\mathbf{r}) = \frac{1}{\beta} \sum_n \sum_{\nu\nu'} \frac{V}{(2\pi)^3} \int d\mathbf{k}\, \psi_{\nu\mathbf{k}}(\mathbf{r}) G_{\nu\nu'}(\mathbf{k}, i\omega_n) \psi^*_{\nu'\mathbf{k}}(\mathbf{r}) \tag{10}$$

$$= \sum_{\nu\nu'} \frac{V}{(2\pi)^3} \int d\mathbf{k}\, \psi_{\nu\mathbf{k}}(\mathbf{r}) n_{\nu\nu'}(\mathbf{k}) \psi_{\nu'\mathbf{k}}(\mathbf{r}), \tag{11}$$

where we used $\psi_{\nu\mathbf{k}}(\mathbf{r}) = \langle \mathbf{r} | \psi_{\nu\mathbf{k}} \rangle$ and also defined the density matrix

$$n_{\nu\nu'}(\mathbf{k}) = \frac{1}{\beta} \sum_n G_{\nu\nu'}(\mathbf{k}, i\omega_n). \tag{12}$$

[2]Note that we are not distinguishing between the (electronic) charge density and the corresponding particle density, i.e., we are using units where the electronic charge is equal to $+1$.

Without considering the self-energy correction, $\Delta\Sigma(\mathbf{k}, i\omega_n)$, in Eq. (5), $G(\mathbf{k}, i\omega_n)$ represents the uncorrected Kohn-Sham Green function, and the corresponding density matrix is diagonal in the KS basis, $n_{\nu\nu'}(\mathbf{k}) \rightarrow n^{\mathrm{KS}}_{\nu\mathbf{k}}\delta_{\nu\nu'}$. Eq. (11) then becomes equivalent to the usual way the charge density is obtained within KS DFT by summing over the occupied KS states, with the only (in practice irrelevant) difference that here the occupations also include a temperature (or β) dependent Fermi-smearing. Otherwise (and apart from a potential additional smearing to improve convergence on a finite $\mathbf{k}$ mesh), the KS occupations, $n^{\mathrm{KS}}_{\nu\mathbf{k}}$ are either one or zero, depending on whether the corresponding KS eigenvalue $\epsilon_{\nu\mathbf{k}}$ is below or above the Fermi level, μ^{KS}, where μ^{KS} is determined by the condition that the number of occupied KS states in the BZ matches the number of electrons in the crystallographic unit cell.

If the self-energy correction is included in Eq. (5), and the full DFT+DMFT lattice Green function is used in Eq. (12), then the resulting density matrix is generally not diagonal any more in the original Kohn-Sham basis. However, for practical implementations, it is often advantageous to define a unitary transformation between all the KS states included in $\mathcal{W}$ that diagonalizes the corrected density matrix at each $\mathbf{k}$ point

$$\sum_{\nu\nu'}[V^{\dagger}(\mathbf{k})]_{\mu\nu}n_{\nu\nu'}(\mathbf{k})V_{\nu'\mu'}(\mathbf{k}) = \tilde{n}_{\mu\mathbf{k}}\delta_{\mu\mu'}\,. \tag{13}$$

Then, the charge density can be calculated from the transformed Bloch functions, $|\tilde{\psi}_{\mu\mathbf{k}}\rangle$, as usual using diagonal occupations

$$\rho(\mathbf{r}) = \sum_{\mu}\frac{V}{(2\pi)^3}\int d\mathbf{k}\,\tilde{n}_{\mu\mathbf{k}}|\tilde{\psi}_{\mu\mathbf{k}}(\mathbf{r})|^2, \tag{14}$$

with

$$\tilde{\psi}_{\mu\mathbf{k}}(\mathbf{r}) = \sum_{\nu}\psi_{\nu\mathbf{k}}(\mathbf{r})V_{\nu\mu}\,. \tag{15}$$

This has the advantage that, after transforming the KS Bloch functions according to Eq. (15), the existing subroutines or functions already included in the DFT code can be used to evaluate the corrected charge density.

In order to ensure full charge self-consistency, another ("outer") iterative loop is added to the computational procedure, as also indicated in Fig. 1, where the KS states and corresponding band energies are recalculated from the KS potential, V_{KS}, evaluated from the corrected charge density obtained from the (inner) DMFT self-consistency loop. In practice, a suitable mixing-scheme is typically applied to ensure or accelerate convergence of the iterative procedure.

If full charge self-consistency is achieved, then the system of electrons, which is divided into a strongly correlated and a weakly correlated part, with the local electron-electron interaction within the correlated subspace explicitly treated within DMFT, and all other interactions incorporated in the KS potential, gives rise to exactly the same density that is used to obtain this KS potential. The KS potential, in turn, defines the KS bandstructure that enters the self-consistent effective bath for the DMFT impurity problem(s).

While this approach appears conceptually reasonable, physically transparent, and, in the charge self-consistent case, also internally consistent, so far the presentation of the DFT+DMFT method

was mostly based on heuristic considerations. However, the DFT+DMFT approach can also be put on a solid theoretical foundation within the conceptual framework of *spectral density functional theory* [9], which is based on an effective action formalism of quantum field theory. A rigorous derivation of the DFT+DMFT approach within this conceptual framework goes beyond the scope of these lecture notes. In the following, we therefore just briefly sketch some of the main ideas.

The starting point is the generic problem of electrons in an external potential, interacting with each other via a Coulombic, i.e., two-particle, interaction. Different approximate treatments of this generic problem can then be constructed by (i) choosing different "observables" to describe the system, (ii) dividing the Gibbs free energy functional into that corresponding to a simpler "reference system" and a remaining "interaction" part, and (iii) finding a good approximation for the interaction part as a functional of the chosen observables. Thereby, the reference system includes a "constraining field" that ensures that the reference system has the same expectation value for the chosen observables as the original interacting electron system. This allows to formulate DFT, DFT+U, and DFT+DMFT all within the same conceptual framework, differing mainly by the choice of the basic observables and the approximations used for the functional representing the unknown part of the interaction energy.

Specifically, DFT is based on the electron density as the central observable and the interaction energy is written as sum of the exactly known Hartree energy and the unknown exchange-correlation energy functional, $E_{\mathrm{xc}}[\rho(\mathbf{r})]$, for which accurate and practically useful approximations exist. The reference system is the system of non-interaction KS electrons and the KS potential takes the role of the constraining field, ensuring that the density of the KS system is identical to that of the original interacting system.

In the case of the DFT+DMFT approach, the local part of the one-particle Green function is chosen as an additional observable, in combination with the electronic charge density, and the interaction part of the Gibbs free energy is written as a sum of the Hartree energy, the usual DFT exchange-correlation energy functional, the interaction energy of the electrons corresponding to the correlated subspace, and a DC correction. The first two terms are functionals of the density, while the last two terms are expressed as functionals of the local Green function. The DMFT approximation then corresponds to considering only purely local diagrams in the evaluation of the interaction energy within the correlated subspace, and the impurity self-energy (or, equivalently, the Weiss field) represents the constraining field for the local Green function.

The formal derivation of the DFT+DMFT approach within the conceptual framework of spectral density functional theory, ensures that the self-consistent solution for the charge density and local Green function correspond to a stationary point of the underlying free energy functional. The total energy within DFT+DMFT can then be obtained by taking the zero temperature limit of the free energy [9]

$$E_{\mathrm{DFT+DMFT}} = E_{\mathrm{DFT}}[\rho(\mathbf{r})] + \langle \hat{H}_{\mathrm{int}} \rangle - E_{\mathrm{DC}}[G^{\mathrm{loc}}] \,. \tag{16}$$

Note that E_{DFT} is usually evaluated within the DFT code and includes the *band energy*, i.e., the total energy of the KS electrons, plus additional terms that are all explicit functionals of

$\rho(\mathbf{r})$. Thus, the total energy reported by the DFT code needs to be corrected for the change in the band energy, by considering the occupations of the KS states according to Eq. (12). The interaction energy within the correlated subspace, $\langle \hat{H}_{\text{int}} \rangle$, can be evaluated using the Galitskii-Migdal formula

$$\langle \hat{H}_{\text{int}} \rangle = \frac{1}{2\beta} \sum_{n,m,m'} \Sigma^{\text{imp}}_{mm'}(i\omega_n)\, G^{\text{loc}}_{m'm}(i\omega_n)\,, \tag{17}$$

and a specific expression for the DC correction E_{DC} is given in Sec. 2.3.

2.3 Local interaction Hamiltonian and double counting correction

There are still two aspects which have been left open up to now. This is the definition of the local interaction Hamiltonian, $\hat{H}_{\text{int}}$, entering the effective DMFT impurity problem, and the question of how to properly define the double counting correction in terms of Σ^{DC} and $E_{\text{DC}}[G^{\text{loc}}]$.
The generic form of a local two-particle interaction, expressed in the local orbital basis of the correlated subspace, is given by

$$\hat{H}_{\text{int}} = \frac{1}{2} \sum_{\{m\}\sigma\sigma'} U_{mm'm''m'''}\, \hat{c}^\dagger_{m\sigma} \hat{c}^\dagger_{m''\sigma'} \hat{c}_{m'''\sigma'} \hat{c}_{m'\sigma}\,, \tag{18}$$

where $\hat{c}^\dagger_{m\sigma}$ is the creation operator corresponding to an electron in orbital $|\phi_{m\mathbf{T}}\rangle$ with spin σ. Note that we have used spin-independent local orbitals, and all creation and annihilation operators in Eq. (18) are meant to correspond to the same site, so that we can drop the index $\mathbf{T}$ for simplicity and we can interpret the index m as indicating only the corresponding orbital character. The matrix elements $U_{mm'm''m'''}$ are defined as

$$U_{mm'm''m'''} = \int d\mathbf{r} \int d\mathbf{r}'\, \phi^*_m(\mathbf{r}) \phi^*_{m''}(\mathbf{r}')\, V_{\text{ee}}(\mathbf{r},\mathbf{r}')\, \phi_{m'}(\mathbf{r}) \phi_{m'''}(\mathbf{r}')\,, \tag{19}$$

where $V_{\text{ee}}(\mathbf{r},\mathbf{r}')$ represents the (screened) local electron-electron interaction experienced by the electrons within the correlated subspace.
In practice, one usually uses a simplified parametrization for the interaction tensor $U_{mm'm''m'''}$. Specifically, for the examples discussed in Sec. 4, a so-called Kanamori parametrization is used (see, e.g., Ref. [10]), which contains only two independent parameters U and J, representing the average inter-orbital Coulomb interaction and the local Hund's exchange, respectively, and the interaction Hamiltonian becomes

$$\begin{aligned} \hat{H}_{\text{int}} = U \sum_m \hat{n}_{m\uparrow}\hat{n}_{m\downarrow} + (U-2J) \sum_{m\neq m'} \hat{n}_{m\uparrow}\hat{n}_{m'\downarrow} + (U-3J) \sum_{m\neq m',\sigma} \hat{n}_{m\sigma}\hat{n}_{m'\sigma} \\ -J \sum_{m\neq m'} \hat{c}^\dagger_{m\uparrow}\hat{c}_{m\downarrow}\hat{c}^\dagger_{m'\downarrow}\hat{c}_{m'\uparrow} + J \sum_{m\neq m'} \hat{c}^\dagger_{m\uparrow}\hat{c}^\dagger_{m\downarrow}\hat{c}_{m'\downarrow}\hat{c}_{m'\uparrow}\,, \end{aligned} \tag{20}$$

where, $\hat{n}_{m\sigma} = \hat{c}^\dagger_{m\sigma}\hat{c}_{m\sigma}$. The Kanamori form corresponds to the most general form of $\hat{H}_{\text{int}}$ for the case of a three-fold degenerate t_{2g} or two-fold degenerate e_g subshell within cubic symmetry, but is also used as approximate form in cases where these degeneracies are lifted. Another

parametrization of $\hat{H}_{\text{int}}$ that is often used for calculations involving the full five-orbital d shell, is the so-called Slater parameterization (see, e.g., Refs. [3,4]).
We note that the calculation of realistic materials- and orbital-specific screened interaction parameters, i.e., the calculation of specific values for U and J in Eq. (20), or of the full interaction tensor in Eq. (19), is an active research area (see other lecture notes in this series). To arrive at a potentially quantitative and predictive method, the "first principles" calculation of such screened interaction parameters is of course highly desirable. Nevertheless, it should be noted that sometimes it can also be instructive to vary, e.g., U and J within certain limits to better analyze the underlying physics.
Finally, we also provide the specific form of the DC correction that was used in the DFT+DMFT calculations discussed in Sec. 4. Generally, an exact definition of $E_{\text{DC}}[G^{\text{loc}}]$ is ill-defined. The DFT exchange correlation functional is a complicated functional of the total density, that does not allow to simply separate off the contributions corresponding to the local interaction of the correlated subspace. Therefore, in practice, heuristic forms are used to account for the DC correction. A widely used form, also used in the examples discussed in Sec. 4, is based on the so-called "fully localized limit" [11, 12], which assumes $E_{\text{DC}} = \frac{\bar{U}}{2} N(N-1)$, where N is the total number of electrons occupying the correlated subspace on the corresponding site, and $\bar{U}$ is the local interaction strength averaged over all orbitals and spins. The corresponding self-energy correction is then defined as $\Sigma^{\text{DC}}_{mm'} = \frac{\delta E_{\text{DC}}}{\delta n_{mm'}} = U\big(N-\frac{1}{2}\big)\,\delta_{mm'}$, where $n_{mm'}$ represents the local density matrix within $\mathcal{C}$. For more details, see, e.g., Ref. [12].

3 Transition metal oxides in a nutshell

In this section, we briefly summarize some basic properties of TM oxides that are important to better understand the materials-specific examples discussed in the next section. In fact, many aspects of TM oxides and related TM compounds can be understood from some simple general considerations about their electronic structure.
The electronic bands around the Fermi level (or around the insulating gap) that govern the low energy properties of TM oxides are usually dominated by states with strong TM d and O p orbital character and can be understood to emerge from the heteropolar covalent bonds formed by the corresponding atomic orbitals. In a somewhat simplified but intuitive picture, this band formation can be understood as a two-step process. First, the hybridization between atomic TM d and O p orbitals gives rise to molecular-orbital-like states located around the corresponding ionic sites, as shown schematically in Fig. 2. Then, the molecular-orbital-like states at different sites hybridize to form extended Bloch states, leading to an energetic broadening of the molecular-orbital-like levels into wider "energy bands".
The energy difference between the atomic TM d and O p states is called the *charge transfer energy*. In most cases, the TM d states are higher in energy than the O p states, corresponding to a positive charge transfer energy. However, the charge transfer energy generally decreases from the lighter to the heavier TM cations in the same row of the periodic table, and thus some nickelates or cuprates can also be characterized as negative charge transfer systems. For a

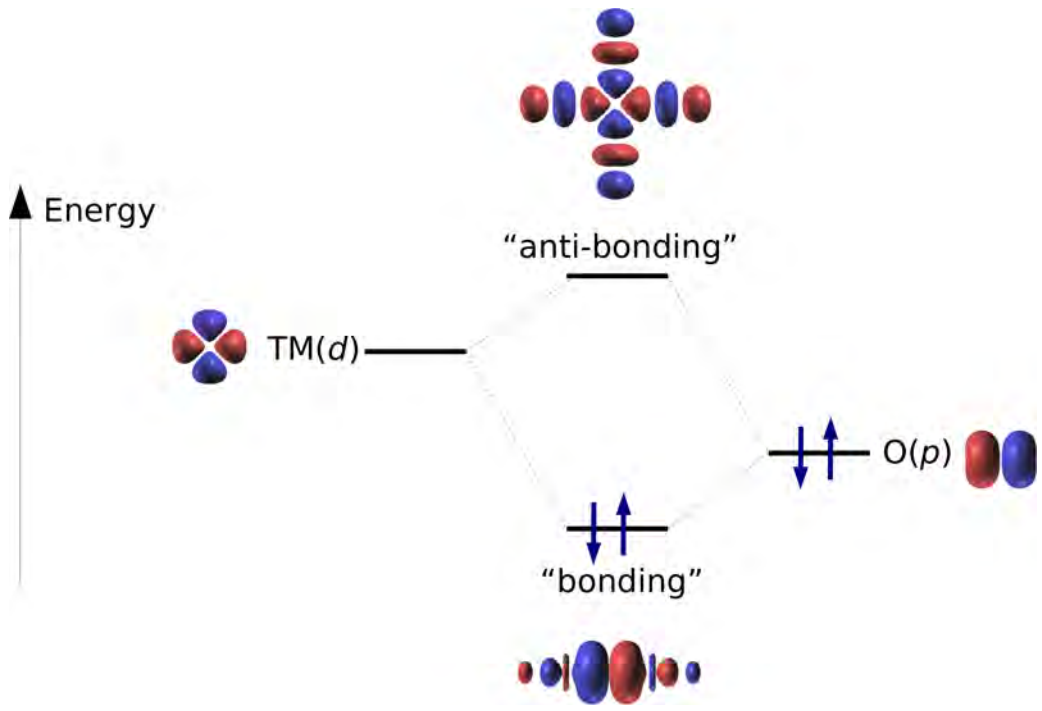

Fig. 2: *Schematic depiction of the formation of a heteropolar covalent bond between atomic orbitals with TM d and O p character, leading to "anti-bonding" and "bonding" molecular-orbital-like states. The depicted orbitals are Wannier functions obtained for $SrVO_3$ by considering different energy windows containing the corresponding bands (see Fig. 3 and the description in the main text).*

positive charge transfer energy, the higher-lying molecular-orbital-like states formed from the hybridization between TM d and O p states have a larger contribution of the TM d atomic orbitals and correspond to an anti-bonding linear combination of the two types of atomic orbitals, while the lower-lying states are dominated by O p contributions and correspond to a bonding combination.

If the charge transfer energy is large enough compared to the width of the bands that form from the overlap or "hopping" between the molecular-orbital-like states located at different sites, then the corresponding bands remain isolated from each other energetically, and can be clearly assigned to the different orbital characters. Fig. 3(a) shows the example of the cubic perovskite $SrVO_3$, with clearly separated groups of bands corresponding, from lower to higher energies, to a dominant O p, V t_{2g}, and V e_g orbital character, respectively (indicated in purple, red, and green in Fig. 3(a)). Note that typically, if one refers for example to the "t_{2g} bands" in $SrVO_3$, then one in fact refers to the group of bands with dominant V t_{2g} orbital character that correspond to the anti-bonding states resulting from the hybridization between atomic V t_{2g} and O p orbitals.

If one now constructs Wannier functions separately from the different groups of bands in Fig. 3(a), using atomic orbitals with the corresponding dominant orbital character as the initial trial orbitals, the resulting Wannier functions exactly resemble the molecular-orbital-like states discussed above for the corresponding group of bands. This is schematically depicted in

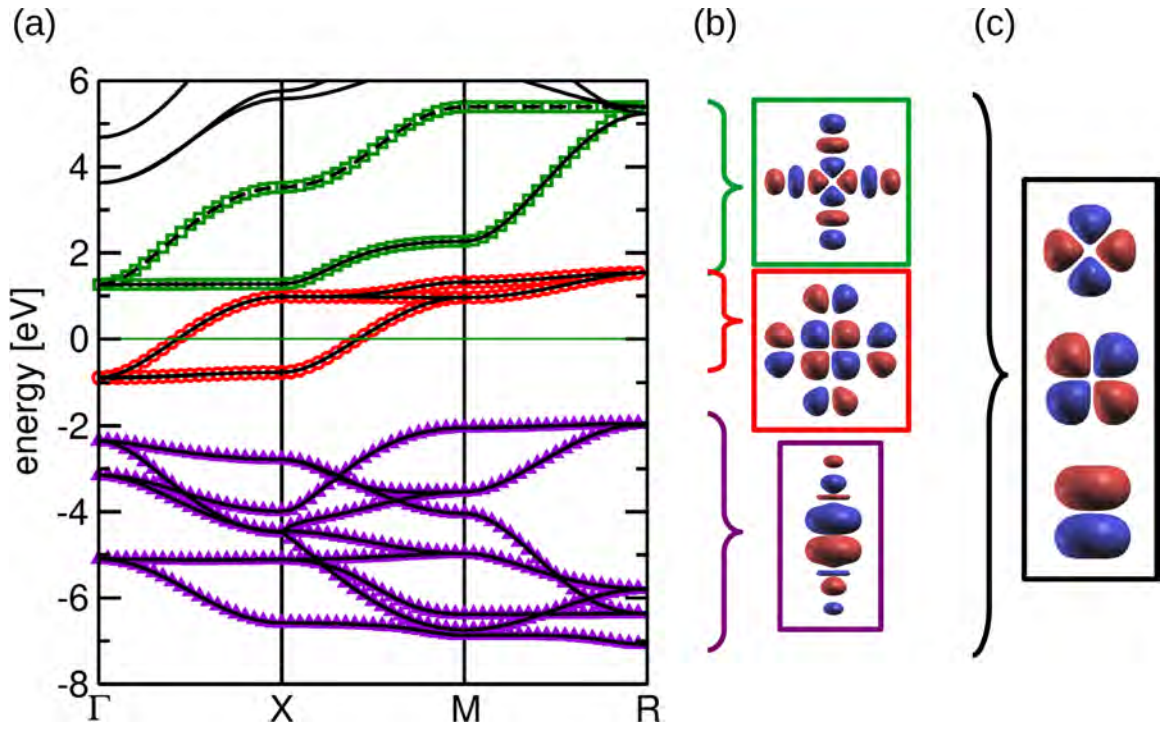

Fig. 3: *(a) KS band structure of $SrVO_3$. The dominant orbital characters of the different isolated groups of bands are indicated by colors, with purple, red, and green corresponding to O p, V t_{2g}, and V e_g dominated bands. (b) and (c) indicate typical Wannier functions obtained by either restricting $\mathcal{W}$ to individual groups of bands or defining $\mathcal{W}$ to span the whole energy window of V d and O p dominated bands.*

Fig. 3(b). For example, for the "t_{2g} bands" in $SrVO_3$, the Wannier functions correspond to anti-bonding linear combinations of an atomic t_{2g} orbital centered at the V site and the π-oriented O p orbitals on the surrounding oxygen ligands. The weight of these "oxygen tails" in the Wannier functions generally increases with decreasing energy separation from the O p dominated bands, i.e., they increase with decreasing (positive) charge transfer energy.

Often, DFT+DMFT calculations are performed using only a minimal correlated subspace with $\mathcal{C} = \mathcal{W}$ restricted to an isolated group of bands immediately around the Fermi level, e.g., the t_{2g} bands in $SrVO_3$. The Wannier orbitals that span the corresponding "frontier" bands are sometimes (and in the following) referred to as "frontier orbitals".

Alternatively, one can also use a Wannier space, $\mathcal{W}$, spanning the whole group of TM d and O p dominated bands. This usually results in Wannier orbitals that closely resemble atomic TM d and O p orbitals,[3] as schematically depicted in Fig. 3(c) for the example of $SrVO_3$. The correlated subspace, $\mathcal{C}$, is then often defined in terms of only the corresponding TM d-like Wannier functions.

[3]Note, however, that Wannier functions in a solid can never strictly be separated in a radial and angular part, as local angular momentum is not a good quantum number.

4 Examples

Before discussing three specific examples for the effect of charge self-consistency, we briefly comment on the case of cubic $SrVO_3$, which is often used as a typical benchmark system to test new DFT+DMFT implementations or extensions to more advanced features. This is related to both its highly symmetric cubic crystal structure as well as its simple and prototypical KS band structure, exhibiting clearly separated groups of bands, as seen in Fig. 3(a). Since the Fermi level cuts through the group of V t_{2g} bands, consistent with the nominal d^1 electron configuration of the V^{4+} cation, one often restricts the Wannier space, $\mathcal{W}$, for the DMFT treatment to only these three V t_{2g} bands (with $\mathcal{C} = \mathcal{W}$), as already discussed in Sec. 3. In this case, the orbital occupations (summed over the two spin projections) are exactly equal to $1/3$, due to the degeneracy of the three t_{2g} levels within cubic symmetry combined with the total filling of the corresponding bands by exactly one electron. Thus, even though a DFT+DMFT calculation will change, e.g., the features of the spectral function compared to the pure DFT treatment, the occupations within the correlated subspace will remain fixed to $1/3$.[4] This means that also the charge density remains identical to the DFT ground state charge density, so that in this case a one-shot calculation is in fact already charge-self-consistent.

Thus, charge self-consistent calculations become only relevant if the occupations are not fixed by the specific symmetry of the system and the total electron count within $\mathcal{C}$. For example, if one extends $\mathcal{W}$ to also include the O p-dominated bands at slightly lower energies, and defines $\mathcal{C}$ in terms of V-centered t_{2g}-like Wannier orbitals constructed from all bands within $\mathcal{W}$, then, even though all three V t_{2g} Wannier orbitals will still have identical occupations due to the cubic symmetry of the system, the total electron count within $\mathcal{C}$ is not fixed any more and electrons can be redistributed between $\mathcal{C}$ and the rest of $\mathcal{W}$ that is not contained in $\mathcal{C}$. This redistribution can then lead to subtle changes in the charge density.

In the following subsections, we focus on two cases where the electron redistribution is more pronounced and leads to noticeable differences between the one-shot results and that of a charge self-consistent DFT+DMFT calculation. All examples employ a definition of the correlated subspace and of the corresponding basis orbitals such that $\mathcal{C} \approx \mathcal{W}$, and $\mathcal{W}$ is isolated from other groups of bands towards lower energies. Thus, since the energy window spanned by $\mathcal{C}$ and $\mathcal{W}$ also includes the Fermi level, the electron count in $\mathcal{C}$ is fixed.[5] The resulting charge redistribution within $\mathcal{C}$ in these examples is therefore always related to the presence of symmetry-inequivalent orbitals or sites.

4.1 Orbital polarization in $CaVO_3$

Our first example is the moderately correlated metal $CaVO_3$, which is closely related to $SrVO_3$. In both materials, the V^{4+} cation exhibits a nominal d^1 electron configuration, but in contrast

[4] Here, we are excluding the possibility of a *spontaneous symmetry breaking* which can always be suppressed in the calculation by appropriate averaging/symmetrizing over equivalent orbitals.

[5] In the examples where $\mathcal{W}$ is not strictly identical to $\mathcal{C}$, the (very) small part of $\mathcal{W}$ that is not included in $\mathcal{C}$ always remains completely unoccupied.

to the perfectly cubic case of $SrVO_3$, the degeneracy of the t_{2g} levels in $CaVO_3$ is lifted due to the orthorhombic distortion of the underlying perovskite crystal structure [see Fig. 4(a)]. The energetic splitting of the t_{2g} levels leads to a (partial) orbital polarization, which is strongly affected by the local interaction and also influences the material's vicinity to a potential Mott metal-insulator transition. This orbital polarization can be further enhanced in thin films of $CaVO_3$ epitaxially grown on a suitable substrate. The mismatch of the lattice constant with that of the substrate material creates a biaxial in-plane strain, which results in a strong additional tetragonal component to the local crystal field on the V sites. Under tensile strain, i.e., if the in-plane lattice constant of the substrate is larger than that of the thin film material, this lowers the energy of the d_{xy} level relative to the other two t_{2g} states. An order-of-magnitude reduction of the resistivity has indeed been reported for $CaVO_3$ thin films grown epitaxially on $SrTiO_3$ [13, 14], for which the corresponding lattice mismatch corresponds to a nominal tensile strain of about 3.5 %.

Fig. 4(c) compares results obtained from charge-self-consistent (CSC) DFT+DMFT calculations with corresponding "one-shot" (OS) calculations for $CaVO_3$ under 4 % tensile epitaxial strain as a function of the local inter-orbital Hubbard interaction U. These calculations have been performed using a basis of three V-centered t_{2g}-like "frontier orbitals" (*cf.* Sec. 3) constructed from the isolated group of bands around the Fermi energy with dominant V t_{2g} character [see Fig. 4(b)].

In both one-shot and charge self-consistent calculations, the system is metallic for small U, indicated by the nonzero spectral weight around zero frequency, evaluated as $\bar{A}(0)=-\frac{\beta}{\pi}\mathrm{Tr}[G(\beta/2)]$, and shown in the lower panel of Fig. 4(c). With increasing U, the system then exhibits a transition to an insulating state, indicated by $\bar{A}(0) \approx 0$. The critical U for this metal-insulator transition is 0.3 eV larger in the charge self-consistent calculation compared to the one-shot result. This increase in the critical U can be related to a strong suppression of the orbital polarization, visible in the upper panel of Fig. 4(c). In the one-shot case, the system becomes nearly completely polarized in the insulating state, with one of the three t_{2g} orbitals nearly completely filled and the other two nearly completely empty. In the charge self-consistent calculation, the orbital polarization is much weaker, even though there is still a clear preferential occupation of one orbital compared to the other two. The partial suppression of orbital polarization in the charge self-consistent case can be understood from the fact that a full occupation of one t_{2g} orbital leads to a strong asymmetry in the charge distribution around the V cation, which then increases the Hartree potential for that particular t_{2g} orbital relative to the other two. This, in turn, will partially counteract the strain-related lowering of the corresponding crystal-field level in the KS potential, and thus reduce the orbital polarization relative to the one-shot result.

Even though the difference in the critical U for the metal-insulator transition between the one-shot and charge self-consistent calculation is not very large, the strong reduction of the orbital polarization can be important for an accurate description of, e.g., spectral properties. Furthermore, this example already highlights a general theme that will also be observed in the next example, i.e., that if the local interaction in DMFT tends to "polarize" the system, either locally between orbitals or also in between different sites, the resulting asymmetric or inhomogeneous

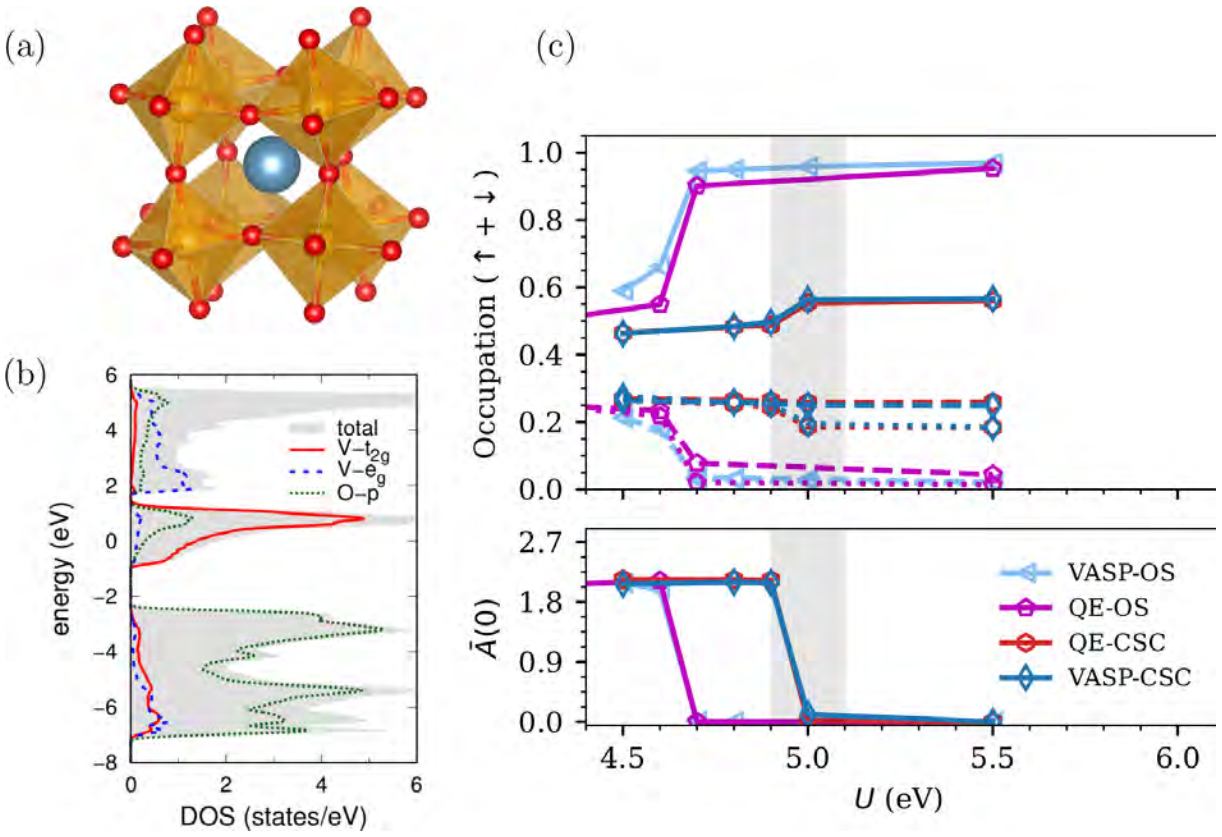

Fig. 4: *(a) Orthorhombically distorted perovskite structure of $CaVO_3$, exhibiting small collective tilts/rotations of the oxygen octahedra around the cubic axes. V atoms and their surrounding coordination octahedra are shown in orange, while O (Ca) atoms are shown in red (blue). (b) KS density of states (DOS) of $CaVO_3$. The total DOS as well as projections on selected atomic orbitals are shown. (c) Spin-summed orbital occupations of the three V t_{2g} frontier orbitals (upper panel), with different orbitals indicated by different line-styles, and zero frequency spectral weight (lower panel) in $CaVO_3$ under 4 % tensile strain obtained from different DFT+DMFT calculations as a function of the Hubbard U. Label QE (VASP) refers to an implementation based on Quantum Espresso (the Vienna Ab-Initio Simulation Package) in combination with TRIQS/solid_dmft [15], while CSC (OS) refers to a charge self-consistent (one-shot) calculation. Subfigure (b) is taken from Ref. [5]. Subfigure (c) courtesy of S. Beck.*

charge distribution is usually disfavored by the strong Hartree interaction included in the KS potential. Consequently, the corresponding polarization is reduced in a charge self-consistent calculation compared to the one-shot case.

Fig. 4(c) also compares two different implementations of the DFT+DMFT self-consistency cycle, one using the "Vienna Ab-Initio Simulation Package" (VASP) and a correlated subspace basis constructed from projection to localized orbitals (PLO) [16], the other based on Quantum ESPRESSO and Wannier orbitals obtained with the Wannier90 code [17]. One can see that the two implementations give nearly identical results, with small differences visible mainly for the orbital occupations in the one-shot case. These small differences can be assigned to the small differences in the definition of the corresponding local orbitals, but the overall quantitative agreement between the two cases is indeed very good.

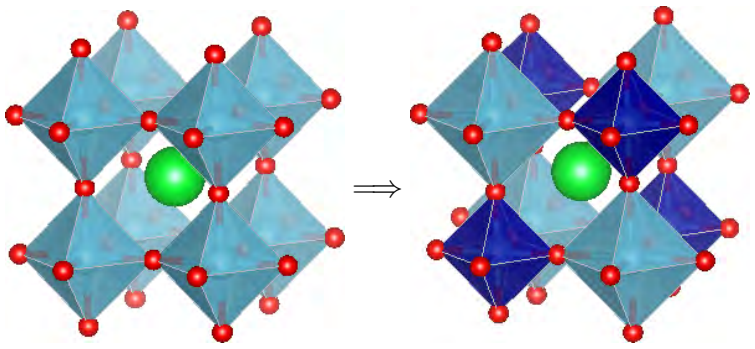

Fig. 5: *Schematic depiction of the octahedral breathing mode distortion of the perovskite structure observed in $CaFeO_3$ and the rare earth nickelates. The oxygen octahedra around the more (less) occupied sites increase (decrease) in volume, resulting in a three-dimensional checkerboard-like spatial arrangement.*

4.2 Potential charge disproportionation in $SrCrO_3$

In the previous example, a charge redistribution occurs between different orbitals centered on the same site. The example discussed in this section involves a charge redistribution between different sites. This is relevant for materials exhibiting *charge ordering* or *charge disproportionation*. Here, we use the former term for a situation where a TM cation has a non-integer average nominal valence, such as, e.g., in magnetite, Fe_3O_4, or in the compositionally doped manganites, $(R,A)MnO_3$, where R is a trivalent rare-earth cation and A a divalent alkaline-earth cation. In contrast, we use the term *charge disproportionation* to refer to situations, where a TM cation has an integer nominal valence, but the corresponding valence state is unfavorable, and can disproportionate into states with higher and lower valence than the average one. One example for a TM oxide exhibiting such charge disproportionation is $CaFeO_3$ [18], where the nominal Fe^{4+} cation disproportionates into a combination of Fe^{3+} and Fe^{5+}, corresponding to a change in the electron configuration according to $2d^4 \rightarrow d^5 + d^3$. Another example is the series of perovskite rare-earth nickelates, $RNiO_3$, where R again indicates a trivalent rare earth cation including also Y and Lu [19]. In this series, the nominal Ni^{3+} cation disproportionates into Ni^{2+} and Ni^{4+}, corresponding to a change in the electron configuration according to $2d^7 \rightarrow d^8 + d^6$.

In both $CaFeO_3$ and the rare earth nickelates, the charge disproportionation occurs below a transition temperature and is accompanied by a metal-insulator transition and a symmetry reduction related to the ordering of the inequivalent disproportionated TM cations on the B sites of the underlying perovskite structure. Furthermore, the disproportionation also couples to a structural distortion that can be understood as a "breathing", i.e., a volume change, of the oxygen octahedra surrounding the inequivalent TM cations, with the octahedra of the more occupied TM cations increasing in volume and the ones corresponding to the less occupied TM cations decreasing (see Fig. 5).

The picture of a "charge" disproportionation in these systems has also been questioned, based on the observation that the actual charge differences, defined, e.g., by integrating the DFT charge density up to some radius within a sphere around the TM sites, is much smaller than the nominal

difference of two electrons. It has therefore been suggested that an interpretation in terms of *ligand holes* could be more appropriate, where the electron configuration around, e.g., the Ni site in $R\mathrm{NiO}_3$ in the undisproportionated state is better described as d^8L, where L represents a hole distributed over the surrounding oxygen ligands. The disproportionation is then interpreted as $2d^8L \rightarrow d^8 + d^8L^2$, with two ligand holes localizing around one of the inequivalent Ni sites. Since the ligand holes are spatially distributed over the surrounding octahedron, the corresponding change in the actual charge density is minimal [20, 21].

Here, we take the viewpoint that, at least in the present context, local charges within a solid are best defined in terms of occupations of suitably defined atom-centered orbitals or Wannier functions. In this case, the ligand hole and "d-only" pictures of electronic disproportionation are just two sides of the same coin, which simply correspond to using different basis sets to describe the same phenomenon. Specifically, a description in terms of a minimal correlated subspace consisting of TM-centered frontier Wannier functions results in orbital occupations that closely resemble the "d-only" picture of charge disproportionation in terms of the formal valence states [22, 23]. On the other hand, a correlated subspace defined in terms of more localized atomic-orbital-like Wannier functions spanning the whole energy window of the TM d and O p dominated bands corresponds more closely to the ligand-hole picture. Since in the following, we analyze DFT+DMFT calculations that employ a frontier orbital basis, we consequently discuss the corresponding results in terms of the d-only picture based on the formal charge states.

Getting back to our example for charge self-consistent DFT+DMFT calculations, we note that in both examples mentioned so far, the disproportionation takes place in the e_g subshell of the TM cation. In the case of the nickelates, the t_{2g} states always remain completely filled and the charge disproportionation can also be described as $2e_g^1 \rightarrow e_g^2 + e_g^0$. Similarly, in CaFeO_3 the Fe always remains in a high-spin state where the t_{2g} orbitals are half-filled with three electrons with the same spin character, and the occupation of the e_g states changes in the same way as in the nickelates.

It is therefore interesting to ask whether charge disproportionation can also occur purely within the t_{2g} subshell. Indeed, model studies considering a generic three-band Hubbard model with an average filling of two electrons per site have found a disproportionated insulating phase in a regime where $U-3J < 0$, i.e., where the local Hubbard interaction is strongly screened while the Hund's interaction remains relatively strong [24, 25]. In this regime, the Hund's interaction dominates over the Hubbard repulsion and it becomes favorable to accumulate a maximum number of electrons with the same spin on the same site, resulting in a charge disproportionation according to $3d^2 \rightarrow 2d^3 + d^0$. The disproportion is thus slightly more complex compared to CaFeO_3 and the nickelates, since the number of d^3 sites is twice the number of empty sites.

Potential candidate materials to observe this physics, are the perovskite chromates $A\mathrm{CrO}_3$, where A can be Ca, Sr, or Pb, and the formal valence of the Cr^{4+} cation corresponds to a d^2 configuration with two electrons in the t_{2g} subshell. In fact, a possible charge disproportionation of the Cr cation has been reported for PbCrO_3 [26, 27], but other reports point more towards a disproportionation of the Pb cations into Pb^{2+} and Pb^{4+}, with all Cr cations in their most fa-

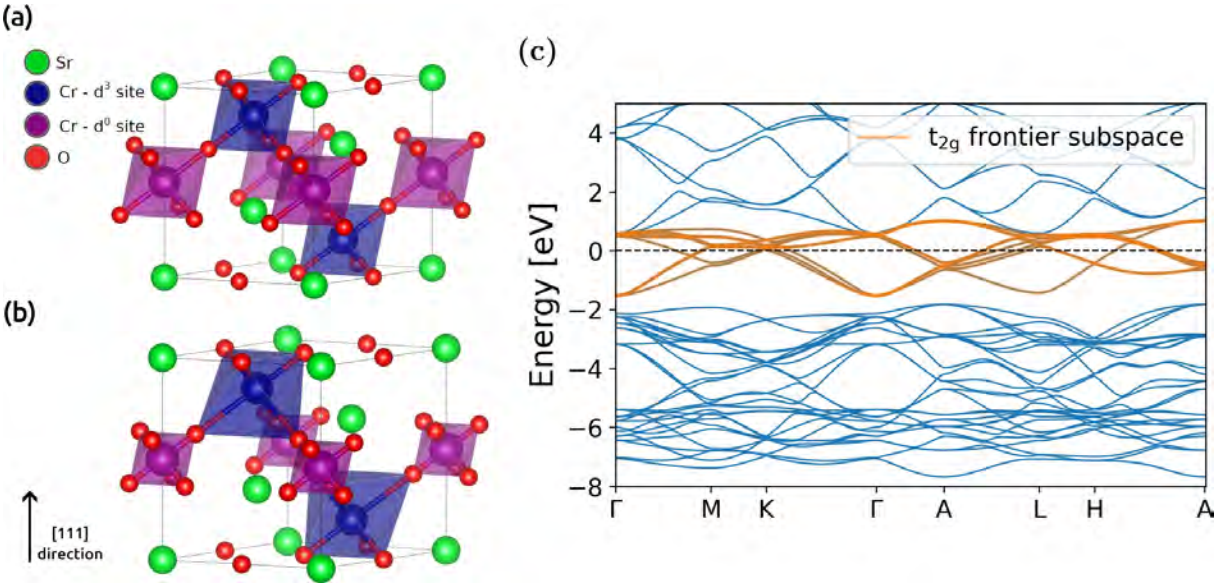

Fig. 6: *(a) Spatial arrangement of the charge disproportionated sites assumed in the DFT+DMFT calculations for $SrCrO_3$, corresponding of a layering along the pseudo-cubic [111] direction, whereby two Cr^{3+} layers (d^3 sites) periodically alternate with one Cr^{6+} layer (d^0 sites), indicated by blue and purple octahedra, respectively. (b) Structural distortion related to the charge disproportionation. The blue Cr^{3+} octahedra expand and distort, while the Cr^{6+} octahedra shrink but essentially keep their perfect octahedral shape. (c) KS bandstructure (blue lines) of cubic $SrCrO_3$ in the energy region around the Fermi level. The orange lines represent the dispersion recalculated from the frontier Wannier functions spanning the correlated Cr t_{2g} subspace. All subfigures are taken from Ref. [35].*

vorable Cr^{3+} oxidation state [28]. Here, we therefore discuss the simpler case of $SrCrO_3$ where the A site cation is definitely divalent, and for which a simple ideal cubic perovskite structure has been reported at ambient conditions. Nevertheless, conflicting experimental reports still exist on the metallic or insulating character of $SrCrO_3$, and on the presence of magnetic order at lower temperatures, see, e.g., Refs. [29–32]. Recently, a potential metal-insulator transition has been reported in thin films of $SrCrO_3$ under tensile strain conditions [33]. While the transition from metallic to insulating behavior under tensile strain can in principle be explained by the emergence of orbital order and a Jahn-Teller distortion [34], a charge disproportionation of the Cr cations could provide an alternative scenario, which has been explored using charge self-consistent DFT+DMFT [35].

The spatial arrangement of potential d^3 and d^0 sites in these DFT+DMFT calculations is depicted in Fig. 6(a). It corresponds to a periodic layering along the [111] direction of the underlying cubic perovskite structure. Two potential d^3 layers are followed by one potential d^0 layer. Here, the term "potential" simply means that the two effective impurity problems corresponding to the potential d^3 and d^0 sites are solved independently (albeit of course coupled through the usual self-consistency condition), and thus allow for a spontaneous electronic symmetry breaking between these otherwise crystallographically equivalent sites. Fig. 6(c) shows the KS band structure of cubic $SrCrO_3$ in the corresponding supercell, with the correlated Cr t_{2g} frontier sub-

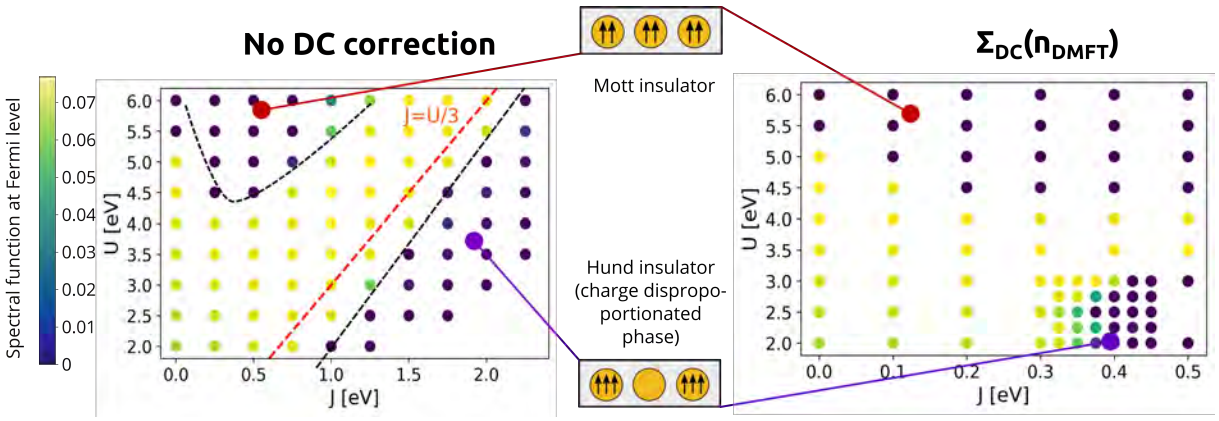

Fig. 7: *Spectral weight around zero frequency, $\bar{A}(0)$, as function of interaction parameters U and J, obtained from different DFT+DMFT one-shot calculations. The left phase diagram corresponds to using DFT occupations to evaluate the DC correction (which in the present case is equivalent to using no DC correction). For the phase diagram on the right, DMFT occupations are used for the DC correction. The regions corresponding to the homogeneous Mott insulator and the charge-disproportionated insulator are indicated. Figure is adapted from Ref. [35] courtesy of A. Carta.*

space indicated by the band dispersion that was recalculated from the corresponding Wannier functions. One can see that these bands are only minimally entangled with the Cr e_g bands at higher energies, and the essentially perfect match with the underlying KS bands indicates that $\mathcal{C} \approx \mathcal{W}$.

We first discuss the results of the corresponding one-shot calculations shown in Fig. 7, where the spectral weight around zero frequency, $\bar{A}(0)$, is plotted as function of the interaction parameters U and J. Here, one has to face an ambiguity of such one-shot calculations, which is whether the total site occupations used for the DC correction are evaluated from the initial DFT occupations or from the occupations obtained after the DMFT treatment of the local interaction. In the present case, these occupations differ substantially in the charge-disproportionated region of the U-J phase diagram. Specifically, the "DFT occupations" are always identical for all Cr sites, since no charge disproportionation occurs in the DFT calculation and thus all sites remain symmetry-equivalent. On the other hand, in the region of the phase diagram where $U-3J < 0$ and charge disproportionation is obtained within DMFT, the difference in the "DMFT occupations" between the nominal d^3 and d^0 sites is typically $\Delta n > 2.6$. This is rather close to the nominal charge difference of 3 electrons, exemplifying that the frontier orbital treatment indeed maps nearly perfectly on the d-only picture of charge disproportionation based on the formal valence states.

Using DFT occupations to evaluate the DC correction is in this case equivalent to not considering any DC correction at all. Since all Cr sites are equally occupied within DFT, the DC correction results in identical shifts of the local potential of each site, which, in the present frontier orbital treatment with $\mathcal{C} = \mathcal{W}$, is simply absorbed by a rigid shift of the chemical potential. The U-J phase diagram on the left side of Fig. 7, labeled "no DC correction", corresponds to

that case, and is essentially identical to the corresponding phase diagram of a generic three-band Hubbard model [24]. There are two distinct insulating phase indicated by $\bar{A}(0) \approx 0$. The conventional Mott-insulating phase, where all Cr sites are equally occupied by two electrons, appears at large $U \gtrsim 4.5\,\text{eV}$. The critical U for the transition into this Mott-insulating phase decreases with J for $J \lesssim 0.5\,\text{eV}$, then increases with J for larger J (cf. Ref. [10]). In the region with $U-3J < 0$, the charge disproportionated phase appears (which was also termed "Hund's insulator" in Ref. [24]), where two of the Cr sites are occupied by nearly three electrons each and one Cr site is nearly empty. The two insulating phases are separated by a metallic region, which extends along the line $U = 3J$ even to very large U. This is the region of a strongly correlated "Hund's metal" [24, 10].

Using DMFT occupations to evaluate the DC correction leads to drastic changes in the corresponding phase diagram. While the overall topology remains the same as before, with a metallic region separating two distinct insulating regions, the region of the charge-disproportionated insulator now appears at significantly smaller J, and even in regions where $U-3J > 0$ (note the different scales of the J axes of the two phase diagrams in Fig. 7). This reflects the fact that now, as soon as a small difference in occupation of the different sites occurs in the DMFT self-consistency loop, the DC correction further lowers the local potential at the more occupied sites relative to that of the less occupied sites, and thus strongly reinforces the charge disproportionation.

As mentioned, the choice of whether to use DFT or DMFT occupations to evaluate the DC correction is ambiguous in a one-shot calculation. This ambiguity is of course a result of the missing charge self-consistency, and the observation that the two different possible choices lead to rather different results of course indicates a strong redistribution of electrons, which in the end calls for a charge self-consistent calculation. On the other hand, in a charge self-consistent calculation the only physically meaningful occupations are the DMFT occupations. These are also the occupations that determine the charge density used to evaluate the KS potential, and thus there is no ambiguity on the choice of occupations for the DC correction in the charge self-consistent case.

If one calculates an analogous phase diagram to the ones shown in Fig. 7 from charge self-consistent calculations, one finds that the charge-disproportionated insulating region in fact completely disappears from the phase diagram. While the Mott-insulating region, where the DMFT occupations are identical to the DFT ones, remains unaffected by the charge self-consistency, the metallic region now fills up the entire rest of the phase diagram, also in the region where $U-3J < 0$. Thus, similar to the previous example of $CaVO_3$, where the orbital polarization is strongly suppressed by the charge self-consistency, the "site polarization" in $SrCrO_3$ is also suppressed, even to an extent that it completely disappears. The strong charge accumulation around the Cr^{3+} sites after the first DFT+DMFT iteration step (which corresponds to a one-shot calculation using DMFT occupations for the DC correction) leads to a strong increase of the local Hartree potential in the second DFT step, which then strongly opposes the charge disproportionation and restores the homogeneous metallic solution with identical occupation on all sites.

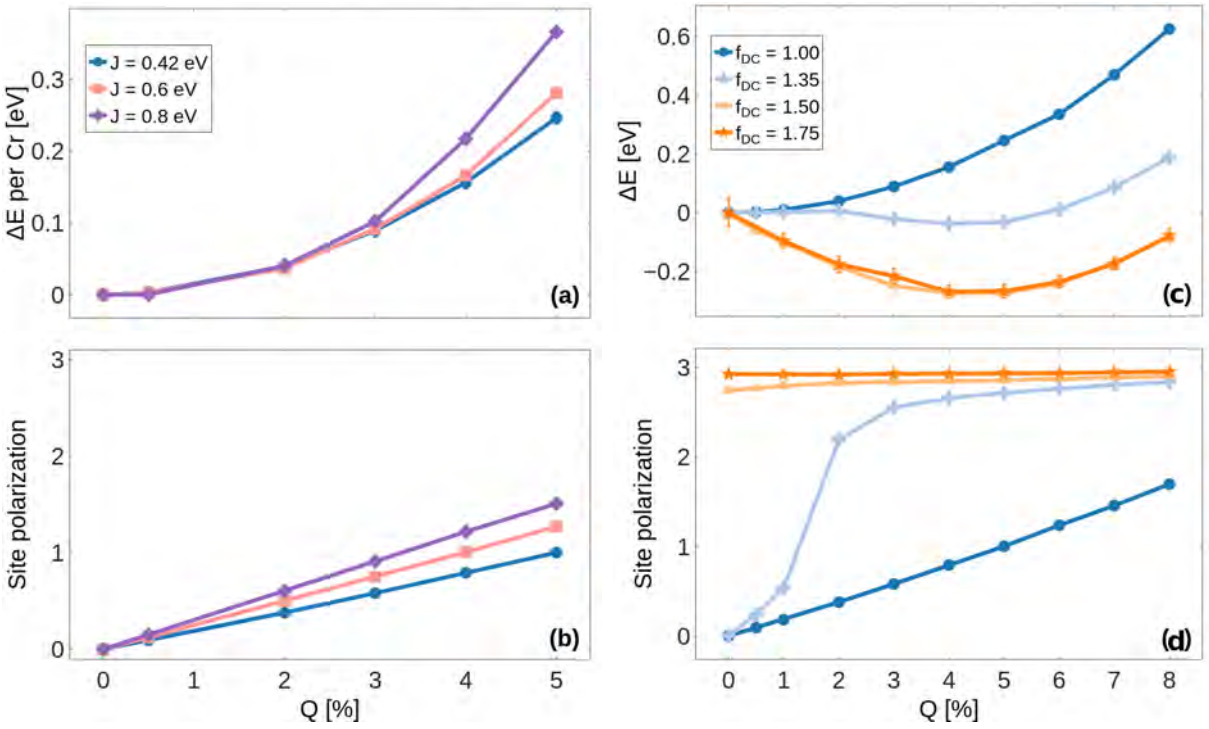

Fig. 8: *Total energy change, (a) and (c), as well as site polarization, (b) and (d), defined as difference in total occupation of the potential d^3 and d^0 sites, obtained from charge self-consistent DFT+DMFT calculations for $SrCrO_3$ as function of the structural breathing mode distortion depicted in Fig. 6(b). The amplitude of the distortion is measured in terms of the change in Cr-O bond length of the smaller octahedra relative to the undistorted case. Panels (a) and (b) are calculated using the standard form of the DC correction, $U = 2.7$ eV, and different values of J. Panels (c) and (d) are calculated using $U = 2.7$ eV, $J = 0.42$ eV, and the DC correction was scaled by f_{DC}. All subfigures are taken from Ref. [35].*

The charge self-consistent calculation thus indicates that $SrCrO_3$ does not exhibit any electronic instability towards spontaneous charge disproportionation.[6] However, as noted previously, in materials such as $CaFeO_3$ and the rare earth nickelates, the charge disproportionation always appears together with a structural distortion corresponding to a breathing of the oxygen octahedra around the TM cations (cf. Fig. 5). This raises the question of whether charge disproportionation in $SrCrO_3$ could also be stabilized by the coupling to an appropriate structural distortion.

An octahedral "breathing mode" compatible with the considered spatial arrangement of potential d^3 and d^0 sites is depicted in Fig. 6(b). Due to the connectivity of the octahedra and the fact that two layers of potential d^3 sites are next to each other, the volume expansion leads to a further distortion of these d^3 octahedra, corresponding to three longer and three shorter Cr^{3+}-O bond distances. On the other hand, the octahedra surrounding the potential d^0 sites can in principle keep their perfect octahedral shape.

Fig. 8 summarizes results of charge self-consistent DFT+DMFT calculations where the ampli-

[6] Since the corresponding region completely disappears from the charge self-consistent phase diagram, we do not even have to face the question which values of U and J would best describe real $SrCrO_3$.

tude of this breathing mode distortion has been varied and both the total energy and the "site polarization, i.e., the difference in total occupation between the nominal d^3 and d^0 sites have been monitored as function of the distortion amplitude. These calculations have been performed for $U = 2.7\,\text{eV}$, which is the value that has been calculated for t_{2g} frontier orbitals in $SrCrO_3$ using the constrained random phase approximation (cRPA) in Ref. [36]. Fig. 8(a) and (b) also shows the effect of varying the strength of the Hund's coupling J, with $J = 0.42\,\text{eV}$ being the calculated cRPA value from Ref. [36]. Note that these cRPA values of $U = 2.7\,\text{eV}$ and $J = 0.42\,\text{eV}$ would put $SrCrO_3$ in the charge disproportionated insulating region according to the one-shot phase diagram on the right side of Fig. 7. On the other hand, the results from the charge self-consistent calculations shown in Fig. 8 show that, even for significantly increased J, the total energy increases essentially quadratically with the structural distortion amplitude, showing no sign of a potential instability towards a distorted charge disproportionated state. This is also consistent with the behavior of the site polarization, which just exhibits an essentially linear response to the structural distortion that breaks the symmetry between the formerly equivalent Cr sites, with no sign of a potential electronic instability.

As discussed above, the DC correction can in principle strongly support a charge disproportionation, by further lowering the local potential of the more occupied sites relative to that of the less occupied sites. On the other hand, the resulting charge accumulation then strongly increases the local Hartree potential if the KS potential is recalculated from the DMFT occupations. Thus, whether charge disproportionation emerges or not, appears to be determined by the subtle balance between these two opposing tendencies. Thereby, one should remember that, as briefly discussed in Sec. 2.3, the DC correction as such is not defined exactly, and that commonly used expressions are mostly based on heuristic arguments and practical experience in their application to different materials systems. In fact, several cases have been identified, where the commonly used expressions for the DC correction do not seem to be completely appropriate, and a scaling of the DC correction is necessary to obtain good agreement with experimental observations [37–39].

Fig. 8(c) and (d) therefore show results of additional charge self-consistent calculations, where the DC correction is scaled by a factor $f_{\text{DC}} > 1$, while U and J are kept fixed to the cRPA values. It can be seen that for $f_{\text{DC}} = 1.35$, the simple linear response of the site polarization to the structural distortion is significantly altered, and a second minimum of the total energy appears for nonzero distortion. In this case, the site polarization exhibits a strong nonlinear increase for distortion amplitudes in the range 1–2 %, to values above 2 electrons, and then saturates for larger distortion to a value slightly below 3. The strong nonlinear increase of the site polarization is accompanied by a transition from metallic to insulating behavior in the spectral functions (not shown). Thus, scaling the DC correction by 35 % puts the system into a regime where the coupling between the structural distortion and the electronic instability stabilizes the charge disproportionated insulating state. For larger scaling, $f_{\text{DC}} \geq 1.5$, the electronic charge disproportionation even occurs again for zero structural distortion (as in the one-shot case), but the minimum of the total energy for nonzero distortion amplitude indicates that this will also stabilize a significant structural distortion.

So what can we finally learn from this example of potential charge disproportionation in $SrCrO_3$? First, it demonstrates nicely and instructively the effect of charge self-consistency, in particular the potential interplay between the DC correction and the change in the Hartree part of the KS potential due to the electron redistribution within DMFT. In the present case, this leads to a clear and rather drastic difference between the charge self-consistent calculation and the corresponding one-shot result. To some extent, the example also exposes the limitations of the current quantitative predictive capabilities of the DFT+DMFT approach, in this case related mostly to the conceptual difficulties in accurately defining the DC correction. On the other hand, even in view of this uncertainty, a required scaling of the DC correction by 35 % relative to the conventional expression appears relatively large, and thus an emergence of charge disproportionation in bulk stoichiometric $SrCrO_3$ is probably unlikely. Nevertheless, the calculations clearly show that $SrCrO_3$ is in fact on the verge of several electronic instabilities (also considering the possibility of orbital order and an accompanying Jahn-Teller distortion explored in Ref. [34]). This observation can provide a possible explanation for the partly conflicting experimental reports regarding its electronic and magnetic properties [29–32], and suggests the possibility to potentially tune $SrCrO_3$ into different insulating ground states by applying strain, substitutional doping, or nano-structuring.

5 Summary and conclusions

In these lecture notes, we have addressed the effect of charge self-consistency in DFT+DMFT calculations, with a special emphasis on TM oxides and related compounds. We have mostly focussed on the practical implementation of the different steps in the iterative computational procedure, summarized by the schematic workflow shown in Fig. 1, but we have also mentioned that the method can be derived rigorously as a stationary solution of a specific approximation to the Gibbs free energy functional in terms of the charge density and the local Green function corresponding to the correlated subspace.

An important aspect of the charge self-consistent procedure is a clear and transparent definition of the local orbitals that span the correlated subspace, which allows to downfold, respectively upfold, various quantities from the KS Bloch basis to the correlated subspace and vice versa. The effect of the DMFT treatment of the local interaction within the correlated subspace is then incorporated in the charge density via the upfolded DMFT occupations defined in Eq. (12). Thus, if these occupations change significantly compared to the initial DFT occupations, a charge self-consistent calculation is generally required.

The two examples discussed in Sec. 4 demonstrate that this is particular relevant in cases where electrons are redistributed within the correlated subspace, either between different non-degenerate orbitals on the same site or between different symmetry-inequivalent sites. This can then result in a strong competition between the tendency of the local correlations to favor an inhomogeneous distribution of electrons and the electrostatic Hartree interaction favoring a more homogeneous distribution.

All specific examples discussed in these lecture notes were based on a definition of the correlated subspace in terms of more or less isolated frontier bands, such that electrons can only be redistributed *within* the correlated subspace. Due to the significantly larger computational effort, charge self-consistent calculations based on a wider energy window, where $\mathcal{W}$ includes also, e.g., the bands with dominant O p character, and $\mathcal{C}$ includes all five d orbitals on the TM site, are sparse. In this case, an electron redistribution can also occur between $\mathcal{C}$ and the uncorrelated part of $\mathcal{W}$, and the DC correction also affects the energy difference between the TM d orbitals and the ligand states. In fact, it has been reported that in several such cases a similar scaling of the DC correction as described in Sec. 4.2 (albeit with $f_{\mathrm{DC}} < 1$) is required to obtain results that are consistent with experimental observations [38, 39]. However, a very recent report indicates that this might also be related to the fact that typically only the TM d orbitals are included in $\mathcal{C}$, while the ligand states remain uncorrected with respect to their KS energies obtained on the DFT level (using approximate semi-local exchange correlation functionals) [40]. Furthermore (to the best of the author's knowledge), no systematic studies on the effect of the charge density update (and its potential interplay with the effect of the DC correction) have been performed for DFT+DMFT calculations using a wide energy window, in particular not for systems involving a charge redistribution both within $\mathcal{C}$ and in between $\mathcal{C}$ and $\mathcal{W} \setminus \mathcal{C}$. Thus, there is still much to be learned on the effect of charge self-consistency and its importance to specific cases.

References

[1] A. Georges, G. Kotliar, W. Krauth, and M.J. Rozenberg, Rev. Mod. Phys. **68**, 13 (1996)

[2] V.I. Anisimov, A.I. Poteryaev, M.A. Korotin, A.O. Anokhin, and G. Kotliar, J. Phys.: Condens. Matter **9**, 7359 (1997)

[3] V.I. Anisimov, F. Aryasetiawan, and A.I. Lichtenstein, J. Phys.: Condens. Matter **9**, 767 (1997)

[4] B. Himmetoglu, A. Floris, S. de Gironcoli, and M. Cococcioni, Int. J. Quantum Chem. **114**, 14 (2014)

[5] S. Beck, G. Sclauzero, U. Chopra, and C. Ederer, Phys. Rev. B **97**, 075107 (2018)

[6] F. Lechermann, in W. Andreoni and S. Yip (Eds.): *Handbook of Materials Modeling* (Springer Cham, 2020), pp. 1099–1118

[7] J. Souto-Casares, N.A. Spaldin, and C. Ederer, Phys. Rev. Res. **3** (2021)

[8] N. Marzari, A.A. Mostofi, J.R. Yates, I. Souza, and D. Vanderbilt, Rev. Mod. Phys. **84**, 1419 (2012)

[9] G. Kotliar, S.Y. Savrasov, K. Haule, V.S. Oudovenko, O. Parcollet, and C.A. Marianetti, Rev. Mod. Phys. **78**, 865 (2006)

[10] A. Georges, L. de' Medici, and J. Mravlje, Annu. Rev. Condens. Matter Phys. **4**, 137 (2013)

[11] V.I. Anisimov, I.V. Solovyev, M.A. Korotin, M.T. Czyżyk, and G.A. Sawatzky, Phys. Rev. B **48**, 16929 (1993)

[12] K. Held, Adv. Phys. **56**, 829 (2007)

[13] M. Gu, J. Laverock, B. Chen, K.E. Smith, S.A. Wolf, and J. Lu, J. App. Phys. **113**, 133704 (2013)

[14] D.E. McNally, X. Lu, J. Pelliciari, S. Beck, M. Dantz, M. Naamneh, T. Shang, M. Medarde, C.W. Schneider, V.N. Strocov, E.V. Pomjakushina, C. Ederer, M. Radovic, and T. Schmitt, npj Quantum Mater. **4**, 6 (2019)

[15] M.E. Merkel, A. Carta, S. Beck, and A. Hampel, J. Open Source Software **7**, 4623 (2022)

[16] M. Schüler, O.E. Peil, G.J. Kraberger, R. Pordzik, M. Marsman, G. Kresse, T.O. Wehling, and M. Aichhorn, J. Phys.: Condens. Matter **30**, 475901 (2018)

[17] S. Beck, A. Hampel, O. Parcollet, C. Ederer, and A. Georges, J. Phys.: Condens. Matter **34**, 235601 (2022)

[18] M. Takano, N. Nakanishi, Y. Takeda, S. Naka, and T. Takada,
Mater. Res. Bull. **12**, 923 (1977)

[19] S. Catalano, M. Gibert, J. Fowlie, J. Íñiguez, J.-M. Triscone, and J. Kreisel,
Rep. Prog. Phys. **81**, 046501 (2018)

[20] H. Park, A.J. Millis, and C.A. Marianetti, Phys. Rev. Lett. **109**, 156402 (2012)

[21] S. Johnston, A. Mukherjee, I. Elfimov, M. Berciu, and G.A. Sawatzky,
Phys. Rev. Lett. **112**, 106404 (2014)

[22] A. Subedi, O.E. Peil, and A. Georges, Phys. Rev. B **91**, 075128 (2015)

[23] M.E. Merkel and C. Ederer, Phys. Rev. B **104**, 165135 (2021)

[24] A. Isidori, M. Berović, L. Fanfarillo, L. de' Medici, M. Fabrizio, and M. Capone,
Phys. Rev. Lett. **122**, 186401 (2019)

[25] S. Ryee, P. Sémon, M.J. Han, and S. Choi, npj Quantum Mater. **5**, 19 (2020)

[26] J. Cheng, K.E. Kweon, S.A. Larregola, Y. Ding, Y. Shirako, L.G. Marshall, Z.-Y. Li,
X. Li, A.M. dos Santos, M.R. Suchomel, K. Matsubayashi, Y. Uwatoko, G.S. Hwang,
J.B. Goodenough, and J.-S. Zhou, Proc. Natl. Acad. Sci. **112**, 1670 (2015)

[27] J. Zhao, S.-C. Haw, X. Wang, L. Cao, H.-J. Lin, C.-T. Chen, C.J. Sahle, A. Tanaka,
J.-M. Chen, C. Jin, Z. Hu, and L.H. Tjeng, Phys. Rev. B **107**, 024107 (2023)

[28] R. Yu, H. Hojo, T. Watanuki, M. Mizumaki, T. Mizokawa, K. Oka, H. Kim, A. Machida,
K. Sakaki, Y. Nakamura, A. Agui, D. Mori, Y. Inaguma, M. Schlipf, K.Z. Rushchanskii,
M. Ležaić, M. Matsuda, J. Ma, S. Calder, M. Isobe, Y. Ikuhara, and M. Azuma,
J. Am. Chem. Soc. **137**, 12719 (2015)

[29] J.-S. Zhou, C.-Q. Jin, Y.-W. Long, L.-X. Yang, and J.B. Goodenough,
Phys. Rev. Lett. **96**, 046408 (2006)

[30] L. Ortega-San-Martin, A.J. Williams, J. Rodgers, J.P. Attfield, G. Heymann, and
H. Huppertz, Phys. Rev. Lett. **99**, 255701 (2007)

[31] A.C. Komarek, T. Möller, M. Isobe, Y. Drees, H. Ulbrich, M. Azuma,
M.T. Fernández-Díaz, A. Senyshyn, M. Hoelzel, G. André, Y. Ueda,
M. Grüninger, and M. Braden, Phys. Rev. B **84**, 125114 (2011)

[32] Y. Long, L. Yang, Y. Lv, Q. Liu, C. Jin, J. Zhou, and J.B. Goodenough,
J. Phys: Condens. Matter **23**, 355601 (2011)

[33] G. Bertino, H.-C. Hsing, A. Gura, X. Chen, T. Sauyet, M. Liu, C.-Y. Nam, and M. Dawber,
arXiv:2104.02738

[34] A. Carta and C. Ederer, Phys. Rev. Mater. **6**, 075004 (2022)

[35] A. Carta, A. Panda, and C. Ederer, Phys. Rev. Res. **6**, 023240 (2024)

[36] L. Vaugier, H. Jiang, and S. Biermann, Phys. Rev. B **86**, 165105 (2012)

[37] M. Karolak, G. Ulm, T.W.V. Mazurenko, A. Poteryaev, and A. Lichtenstein, J. Electr. Spectr. Rel. Phenom. **181**, 11 (2010)

[38] H.T. Dang, X. Ai, A.J. Millis, and C.A. Marianetti, Phys. Rev. B **90**, 125114 (2014)

[39] H. Park, A.J. Millis, and C.A. Marianetti, Phys. Rev. B **89**, 245133 (2014)

[40] A. Carta, A. Panda, and C. Ederer, arXiv:2502.17229